

A Comparative Study of Cyclic Oxidation and Sulfates-Induced Hot Corrosion Behavior of Arc-Sprayed Ni-Cr-Ti Coatings at Moderate Temperatures

Wenmin Guo, Yuping Wu, Jianfeng Zhang, Sheng Hong, Liyan Chen, and Yujiao Qin

(Submitted May 28, 2014; in revised form November 26, 2014)

The cyclic oxidation and sulfates-induced hot corrosion behaviors of a Ni-43Cr-0.3Ti arc-sprayed coating at 550–750 °C were characterized and compared in this study. In general, all the oxidation and hot corrosion kinetic curves of the coating followed a parabolic law, i.e., the weight of the specimens showed a rapid growth initially and then reached the gradual state. However, the initial stage of the hot corrosion process was approximately two times longer than that of the oxidation process, indicating a longer preparation time required for the formation of a protective scale in the former process. At 650 °C, the parabolic rate constant for the hot corrosion was $7.2 \times 10^{-12} \text{ g}^2/(\text{cm}^4 \cdot \text{s})$, approximately 1.7 times higher than that for the oxidation at the same temperature. The lower parabolic rate constant for the oxidation was mainly attributed to the formation of a protective oxide scale on the surface of corroded specimens, which was composed of a mixture of NiO, Cr₂O₃, and NiCr₂O₄. However, as the liquid molten salts emerged during the hot corrosion, these protective oxides would be dissolved and the coating was corrupted acceleratedly.

Keywords arc spray, coating, hot corrosion, oxidation

1. Introduction

High temperature oxidation and hot corrosion have been known as significant deterioration processes for engineering materials by limiting the service temperature, the efficiency, and the reliability of the alloy components in waste-, biomass-, coal-fired boilers, gas-turbine engines, petro-plant, and so on. Although these hot-section components could be protected by thermal-sprayed coatings, the selection of appropriate composition and the formation of an ideal morphology are still big challenges for the balance of reducing the cost and providing enough protection. From the view point of oxidation kinetics, alloys with the ability to grow a continuous and compact Cr₂O₃ (chromia) scale are often preferred for enhancing the oxidation or hot corrosion resistance at moderate temperatures (Ref 1). Thus, the concentration of Cr in the coating should be naturally higher than a critical value for the formation of a protective Cr₂O₃ scale (Ref 2). That is the reason that the high Cr content coatings have been considered competitive for the long-term service at mod-

erate temperatures (Ref 3–5). Bala et al. (Ref 6) found that the HVOF and cold-sprayed Ni-20Cr coatings reduced the erosion-corrosion rate of T22 steel by 82 and 56%, respectively, in actual boiler environment. Chatha et al. (Ref 7) reported that the HVOF-sprayed Ni-20Cr coating did not show any internal corrosion attack after 1500 h exposure to coal-fired boiler. Bala et al. (Ref 8) also demonstrated that the cold-sprayed Ni-50Cr coating held a better corrosion resistance than the Ni-20Cr coating in the oxidation environment at 900 °C.

In practical applications, the deterioration of materials is caused not only by oxidation in air, but also from other resources of attack. For example, the presence of sulfates usually accelerates this process by hot corrosion. Wang et al. (Ref 9) investigated the oxidation and hot corrosion behavior of a Ni-based alloy (K52 alloy) and its nano-grained counterpart under molten Na₂SO₄ + 25% K₂SO₄ salt. The results showed that the nanostructured K52 coating led to a greatly reduced oxidation rate at 800–1000 °C. On the contrary, it exhibited a faster hot corrosion rate than the cast K52 alloy at 850 °C. Ren et al. (Ref 10) have investigated the oxidation and hot corrosion behavior in the presence of 75 wt.% + 25 wt.% K₂SO₄/NaCl film of a nanocrystalline Ni-30Cr-8Al-0.5Y coating on a Ni-based superalloy. The results indicated that the coating possessed excellent oxidation resistance at 1000–1100 °C, whereas the coating degenerated completely at the transient hot-corrosion stage in the molten salt film at 900 °C. Similar studies also have been carried on the detonation-gun-sprayed Cr₃C₂-NiCr coating (Ref 11), cold-sprayed Ni-50Cr coating (Ref 12), HVOF Ni-20Cr coating (Ref 13), plasma-sprayed NiCrAlY coating

Wenmin Guo, Yuping Wu, Jianfeng Zhang, Sheng Hong, Liyan Chen, and Yujiao Qin, College of Mechanics and Materials, Hohai University, Nanjing 210098, China. Contact e-mails: wuyuping@hhu.edu.cn, wenminguo@hotmail.com, and jfzhang@hhu.edu.cn.

(Ref 14), etc. Overall, this type of attack is often severe and sometimes even catastrophic. However, the understanding of the complex mechanism for the hot corrosion is still not comprehensive, especially its correlation with oxidation, even though the hot corrosion has been recognized as an accelerated oxidation process.

In the present study, a high Cr content Ni-based coating of Ni-43Cr-0.3Ti was fabricated on AISI 1020 steel by a twin-wire arc spray process. The as-sprayed coating was pre-covered by a $\text{Na}_2\text{SO}_4 + \text{K}_2\text{SO}_4$ (7:3) mixed salt film for the hot corrosion trails. Then the cyclic oxidation and hot corrosion behaviors of the Ni-43Cr-0.3Ti coating at 550–750 °C were characterized and compared, and the related mechanisms were discussed.

2. Experimental Procedures

2.1 Development of Coatings

AISI 1020 steel was used as the substrate in the present investigation. The nominal chemical composition of the substrate material was 0.23 wt.% C, 0.24 wt.% Si, 0.016 wt.% S, 0.012 wt.% P, 0.4 wt.% Mn, and balance Fe. The steel was cut to 30 mm × 10 mm × 8 mm in dimension, and polished by SiC papers down to 150-grit. Then the steel was ultrasonically degreased in acetone, rinsed in alcohol, dried in air, and grit blasted with alumina powders.

The high Cr coating (Ni-43Cr-0.3Ti, Tafa 45 CT) was employed for the high temperature oxidation and hot corrosion test. The Tafa 45 CT wire, which was developed originally from a workable welding filler metal (known as Filler Metal 72 (55Ni44Cr1Ti)), was reported to have the highest chromium content of any wire product (Ref 15). In the present study, the coatings were deposited on the as-prepared AISI 1020 steel with a High-Jet DZ-Arc-500E industrial arc spray system using 1.6-mm diameter wires. A schematic diagram of the electric arc spray process is shown as Fig. 1. All the six sides of the substrate were coated (~300 μm in thickness) with the optimized spray parameters as showed in Table 1.

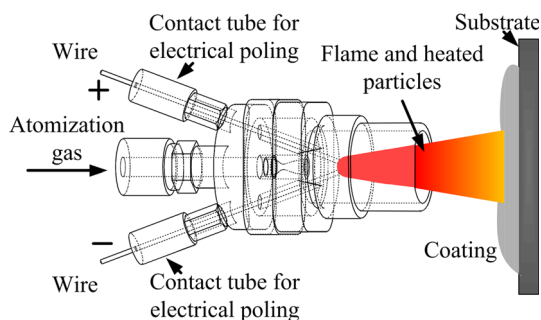


Fig. 1 A schematic diagram of the electric arc spray process

2.2 Characterization

The phase composition of the as-sprayed coating was identified by x-ray diffraction (XRD) patterns using a Bruker AXS D8 Advance diffractometer (Germany) with a Cu $K\alpha$ target at 40 kV and 30 mA. Scans were run at a rate of 4 °/min. For the microstructural observation, the specimens were cut in cross section, mounted in epoxy, and mirror polished. Then the polished specimens were observed by the optical microscope (BX51M, OLYMPUS) and Philips XL30 scanning electron microscope (SEM). The porosity of the coating was evaluated using image analyzer of DT2000 software from the image taken by the optical microscope. Fifteen measurements along the medium position of the coatings were averaged for each reported value.

2.3 Cyclic Oxidation and Hot Corrosion Trials

Cyclic oxidation trials in still air were carried out in a box furnace for 20 cycles at 550, 650, and 750 °C, respectively. Each cycle consisted of 5 h heating at each temperature followed by 20 min cooling to room temperature. Each specimen was kept in a crucible to make sure that the spalled scale was also included during the weight change measurements. Total weight change measurements were taken at the end of each cycle using an electronic balance machine (FA2004N) with a sensitivity of 0.1 mg.

Prior to the hot corrosion trails, a mixture of sulfates ($\text{Na}_2\text{SO}_4\text{-K}_2\text{SO}_4$, 7:3) was properly dissolved in distilled water. Then, a uniform film of $\text{Na}_2\text{SO}_4\text{-K}_2\text{SO}_4$ mixed salt was covered on the preheated specimens (250 °C) with a camel hairbrush so as to have an approximate thickness of 3–5 mg/cm². Subsequently, these salt-covered specimens were kept in a drying oven and heated at 100 °C for 3 h to remove the moisture from the salt film. Similar to cyclic oxidation trials, hot corrosion studies in the molten salt environment under cyclic conditions were performed up to 20 cycles at 550, 650, and 750 °C, respectively. Each specimen was kept in a crucible, and the total weight of the crucible and specimen was measured. After being corroded for 100 h, the specimens were cleaned in boiling water and dried in air.

The corroded specimens were analyzed for the characterization of oxide scales. The analysis was performed for surface and cross section of the exposed specimens with a combination of XRD, SEM, and EDS.

3. Results and Discussion

3.1 Characterization of Arc-Sprayed Coatings

Figure 2 presents the cross-sectional morphologies of the arc-sprayed 45CT coating. The coating showed a typical lamellar structure, consisting of well-transformed bright lamellar structures and dark contrast oxide stringers. The thickness of the bright lamellar structures ranged from thin layers less than 1 μm through to larger bulk

features (Fig. 2b). The oxide stringers were thinner than 5 μm . Some voids and pores were located within the oxide stringers or along the bright lamellar structure/oxide interface. The porosity of the coating is approximately 2.1%. Table 2 shows the electron energy spectrum (EDS) analysis results of bright lamellar structures (labeled as point A) and dark (labeled as point B) or gray (labeled as point C) oxide stringers. The bright lamellar structure was confirmed to be Ni-based (Ni, Cr) solid solution by the EDS analysis. The oxide stringers in the as-sprayed coating could be classified into two categories: most of Cr-rich oxides (dark areas labeled as point B) and small amount of Ni-rich oxides (gray areas labeled as point C). It is in good agreement with that of the optimized coatings in earlier studies (Ref 16). The Cr content in the bright lamellar structures (labeled as point A) was detected as 38.8 wt.%, whereas that in the oxides (labeled as point B and point C) was 46.1 and 29.9 wt.%, respectively. The occurrence of this compositional fluctuation was ascribed to the selective oxidation of Cr and Ni in the molten droplets during arc spray process.

3.2 Kinetic Analysis for High Temperature Corrosion

Figure 3 shows the weight change of the coatings subjected to the cyclic oxidation and hot corrosion at 550–750 $^{\circ}\text{C}$. The curves have two distinct stages: an initial fast weight-gain stage and a second slower-growing stage. The

kinetics for the second stage follows a parabolic rate law. Previous studies (Ref 17) illustrated that the deterioration of the coatings in the initial stages was chemically controlled due to the large thermodynamic driving force available for the formation of all kinds of oxides, including fast-growing NiO. As shown in Fig. 3(a), the weight gain of the NiCrTi coating after oxidation at 550 $^{\circ}\text{C}$ was much lower than that at 650 and 750 $^{\circ}\text{C}$, indicating the best oxidation resistance. Figure 3(b) shows that the parabolic rate constant (k_p) values at 650 $^{\circ}\text{C}$ were $0.43 \times 10^{-11} \text{ g}^2/(\text{cm}^4 \cdot \text{s})$, much lower than $1.19 \times 10^{-11} \text{ g}^2/(\text{cm}^4 \cdot \text{s})$ at 550 $^{\circ}\text{C}$ and $0.95 \times 10^{-11} \text{ g}^2/(\text{cm}^4 \cdot \text{s})$ at 750 $^{\circ}\text{C}$, indicating a lowest increase rate of the weight gain of the corroded samples.

The initial stage in the hot corrosion process was approximately two times longer than that in the oxidation process, indicating that the formation of the protective oxide scale required a longer time (Fig. 3c). As the whole surface of the coating was covered by oxides, the reaction kinetics transformed to a diffusion controlled mode. Figure 3(d) shows the parabolic rate constant (k_p) values of the coating after hot corrosion. It is clear that the coatings exhibited the lowest k_p values at 650 $^{\circ}\text{C}$ whether in the oxidation or hot corrosion process, which indicated the lowest growth of the oxide scales, although a set of repeated oxidation and hot corrosion tests had been carefully performed to make sure the reliability of the research results. At 650 $^{\circ}\text{C}$, the parabolic rate constant for the hot corrosion was $7.2 \times 10^{-12} \text{ g}^2/(\text{cm}^4 \cdot \text{s})$, which was approximately 1.7 times higher than that for the oxidation at the same temperature, indicating that sulfates significantly accelerated the high temperature deterioration process. Actually, the high temperature corrosion resistance of materials depends not only by the environment temperatures, but also by the composition, structure, stability, compactness, and continuity of the protective oxide scales which formed on the surface of corroded specimens. The lowest k_p values of the coating after oxidation or hot corrosion at 650 $^{\circ}\text{C}$ were mainly ascribed to the most compact and smooth protective oxide scales formed on the surface of the corroded specimens, which were demonstrated later.

Table 1 Process parameters for coatings produced by arc spray

Arc spray parameter	Value
Current	180 A
Voltage	36 V
Air pressure	0.65 MPa
Spray distance	200 mm

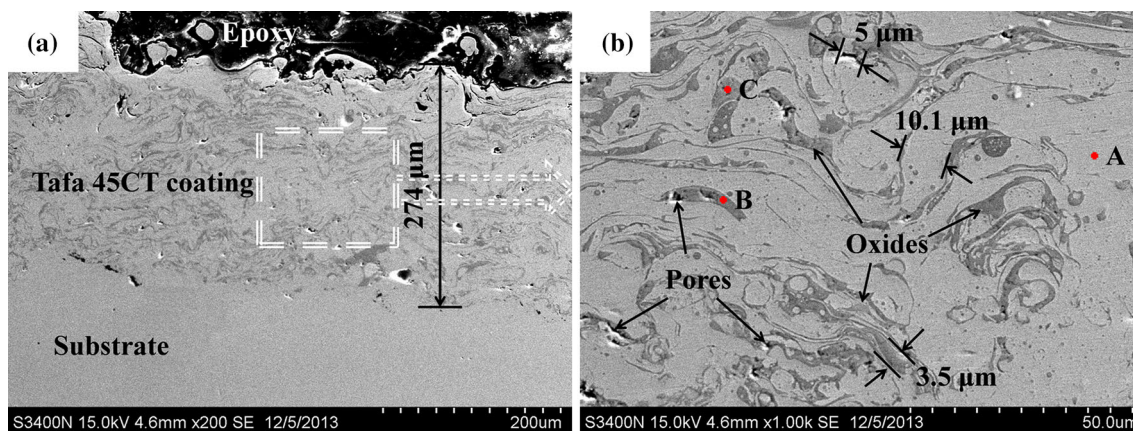


Fig. 2 Cross-sectional morphologies of the as-sprayed 45CT coating

3.3 XRD Analysis

The XRD patterns of the as-sprayed coating and the specimens subjected to cyclic oxidation and hot corrosion at 550–750 °C are depicted in Fig. 4. γ -Ni (JCPDS 70-0989), Cr_2O_3 (JCPDS 38-1479), and NiO (JCPDS 47-1049) were identified to be the main phases in the as-sprayed coating. Besides of these, NiCr_2O_4 (JCPDS 54-0961) was sometimes detected in the protective oxide scales of the corroded specimens. The XRD analysis results were in good agreement with the phases reported by Matthews et al. (Ref 18) and Bala et al. (Ref 6, 8). At 550 °C, the XRD patterns of corroded specimens after oxidation and hot corrosion showed no distinct difference. In addition, no trace of NiCr_2O_4 was detected. At 650 °C, the relative intensity of Cr_2O_3 peaks of corroded specimens after oxidation showed a slight increase than that at 550 °C, indicating that the formation of Cr_2O_3 can be enhanced by

Table 2 The electron energy spectrum (EDS) analysis results corresponding to the positions in Fig. 2(b)

	Element, wt. %		
	Ni K	Cr K	O K
A	53.83	38.81	3.93
B	16.61	46.12	35.21
C	36.93	29.90	31.66

increasing the temperature (Fig. 4a). As showed in Fig. 4(b), the relative intensity of NiO and NiCr_2O_4 peaks of the corroded specimens after hot corrosion at 650 °C increased. However, the relative intensity of γ -Ni peaks was dramatically decreased. This abnormal change may be caused by the high density of oxide grains distribution on the surface of corroded coatings after hot corrosion at 650 °C. These oxide grains were further confirmed to be a mixture of NiO and NiCr_2O_4 by the later EDS analysis. With increasing the temperature up to 750 °C, the relative intensity of Cr_2O_3 and NiCr_2O_4 peaks showed a sustainable growth with temperature increasing. However, the relative intensity of Cr_2O_3 and NiCr_2O_4 peaks in XRD patterns of corroded specimens after hot corrosion was much lower than that after oxidation.

3.4 Surface Analysis of the Oxidized Specimens

The surface morphologies of the corroded specimens after cyclic oxidation and hot corrosion are presented in Fig. 5. All the corroded coatings were covered by continuous oxide scales of overlapping strips, irregularly nodules and/or particles. With increasing the test temperature from 550 to 750 °C, the surface of the corroded coatings appears to be more uneven.

Two distinct regions, a dense one (labeled as I) and a porous one (labeled as II), were observed on the surface of the corroded coating after oxidation at 550 °C, as showed in Fig. 5(a). With increasing the temperature up to 650 °C,

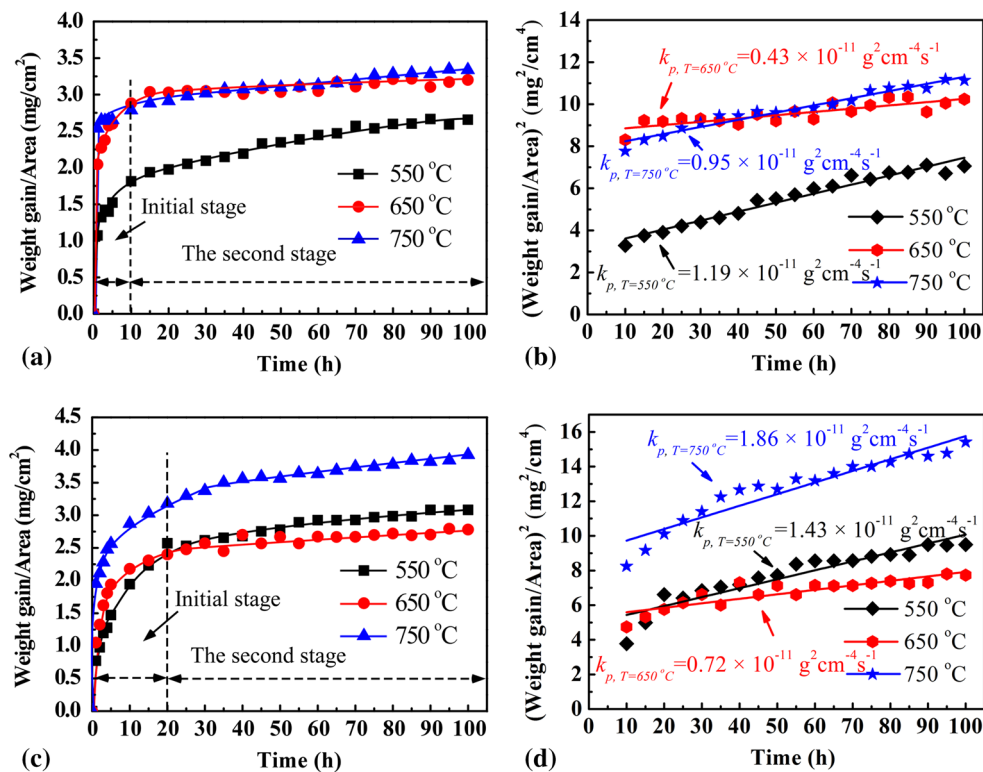


Fig. 3 Weight gain vs. corrosion time ((a) for oxidation, (c) for hot corrosion) and square weight gain vs. corrosion time ((b) for oxidation, (d) for hot corrosion) plots for the specimens subjected to cyclic oxidation in air and hot corrosion under the $\text{Na}_2\text{SO}_4 + \text{K}_2\text{SO}_4$ (7:3) mixed salt film at 550, 650, and 750 °C

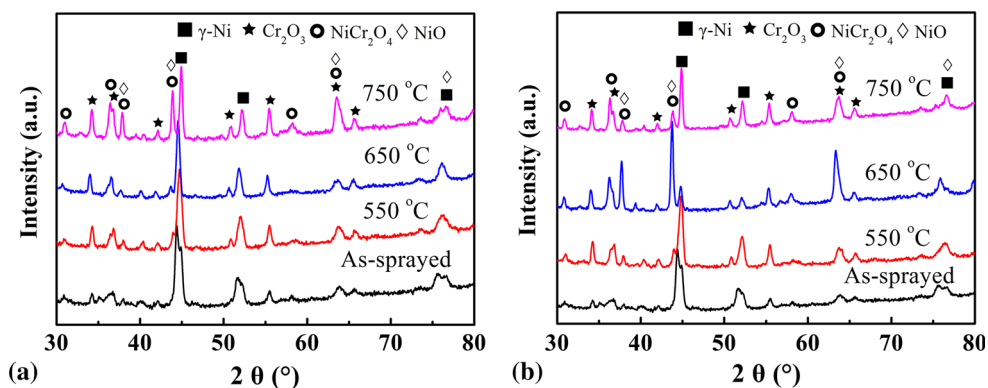


Fig. 4 XRD patterns of the as-sprayed Ni-Cr-Ti coating and the oxide scales formed on the corroded specimens after cyclic oxidation and hot corrosion at 550-750 °C. (a) After oxidation, (b) after hot corrosion

the oxide scale, which was composed of nearly circular-planar structures, appeared to be more dense and smooth (Fig. 5c). The EDS analysis results indicate that the oxide scale has a higher Ni/Cr ratio than that formed at 550 °C. At 750 °C, the exposed coating has a granular appearance in general (Fig. 5e). The average grain size is approximately 1.4 μm , approximately 3 times larger than that formed at 550 °C. The EDS analysis results reveal that the chemical composition of grains is closed to the NiCr_2O_4 spinel structure (labeled as point H in Fig. 5e).

The surface of the corroded specimens after hot corrosion was much more uneven than that after oxidation in air. It consisted of irregularly nodule structures and particles with deep grooves (Fig. 5b, d, and f). The grain size of the irregularly particles is different in different zones. It also shows an increasing tendency as the temperature rise. At 550 °C, the grains can be grouped into two categories: large irregular polyhedrons (labeled as J in Fig. 5b) and small circular platelets (labeled as K in Fig. 5b). EDS analysis of the large irregular polyhedrons shows the significant presence of Ni and Cr along with oxygen indicating the possibility of the formation of NiO and NiCr_2O_4 . EDS analysis of small circular platelets indicates the possibility of the formation of Cr_2O_3 . At 650 °C, the surface shows a more uniform appearance, which was covered by an amount of large irregular polyhedrons (Fig. 5d). At 750 °C, cracks could be observed along the surface of these grains, which was mainly caused by the growth stress and the difference in thermal expansion coefficient of these oxide grains (Fig. 5f).

3.5 Cross-Sectional Analysis of the Scale

Figure 6 shows the cross-sectional morphologies and EDS analysis results of the oxide scale formed on the surface of corroded specimens after cyclic oxidation and hot corrosion at 650 °C. Deep grooves existed at the interface between the oxide scale and epoxy. This is mainly due to the high brittleness of the oxide scales during the preparation of metallographic specimen.

Unlike the oxidation behavior of Ni-Cr alloys in a bulk form (Ref 19, 20), no trace of the internal oxidation has been observed in the bright lamellar structures near the

oxide scale/coating interface. In the protective oxide scales, all the bright lamellar structures have been surrounded by thick oxide strips, indicating that the bright lamellar structures/oxides interface was the preferential pathway for oxidation. EDS analysis results of the oxide scales showed that the variation of the Cr concentration always keeps consistent with that of O and were contrary to that of Ni (Fig. 6c). The residual bright lamellar structures in the oxide scales always correspond with a high concentration of Ni, implying that the rapid depletion of Cr results in the enrichment of Ni in the bright lamellar structures.

There are great differences between the cross-sectional morphologies of 45 CT coatings subjected to cyclic oxidation and hot corrosion (Fig. 6). First, the thickness of the oxide scales after hot corrosion was much higher than that after oxidation, indicating that the interface of bright lamellar structures and oxides was easier to be corroded in hot corrosion than that in oxidation. Second, plenty of pores are generated near the oxide/coating interface in the protective oxide scales formed in hot corrosion process, which is mainly due to the rapid outward-diffusion of metal atoms (Ref 21). However, pores in the protective oxide scales after oxidation always exist near the oxide scale/air interface, which formed mainly due to corrosion of metals caused by the inward-diffusion of oxygen (Ref 22, 23). The porosity of the protective oxide scales formed on the corroded specimens after hot corrosion was measured to be 3.2%, much higher than 2.5% after oxidation.

4. Discussion

4.1 Oxidation

Figure 7 presents the schematic oxidation and hot corrosion models for arc-sprayed Ni-Cr coatings. The oxidation mechanism of Ni-Cr alloys has also been widely elaborated in the literature (Ref 8). In the initial stage of oxidation, NiO and Cr_2O_3 formed on the exposed surface of specimens, but the growth speed of the former is higher than that of the latter. Therefore, a NiO scale would

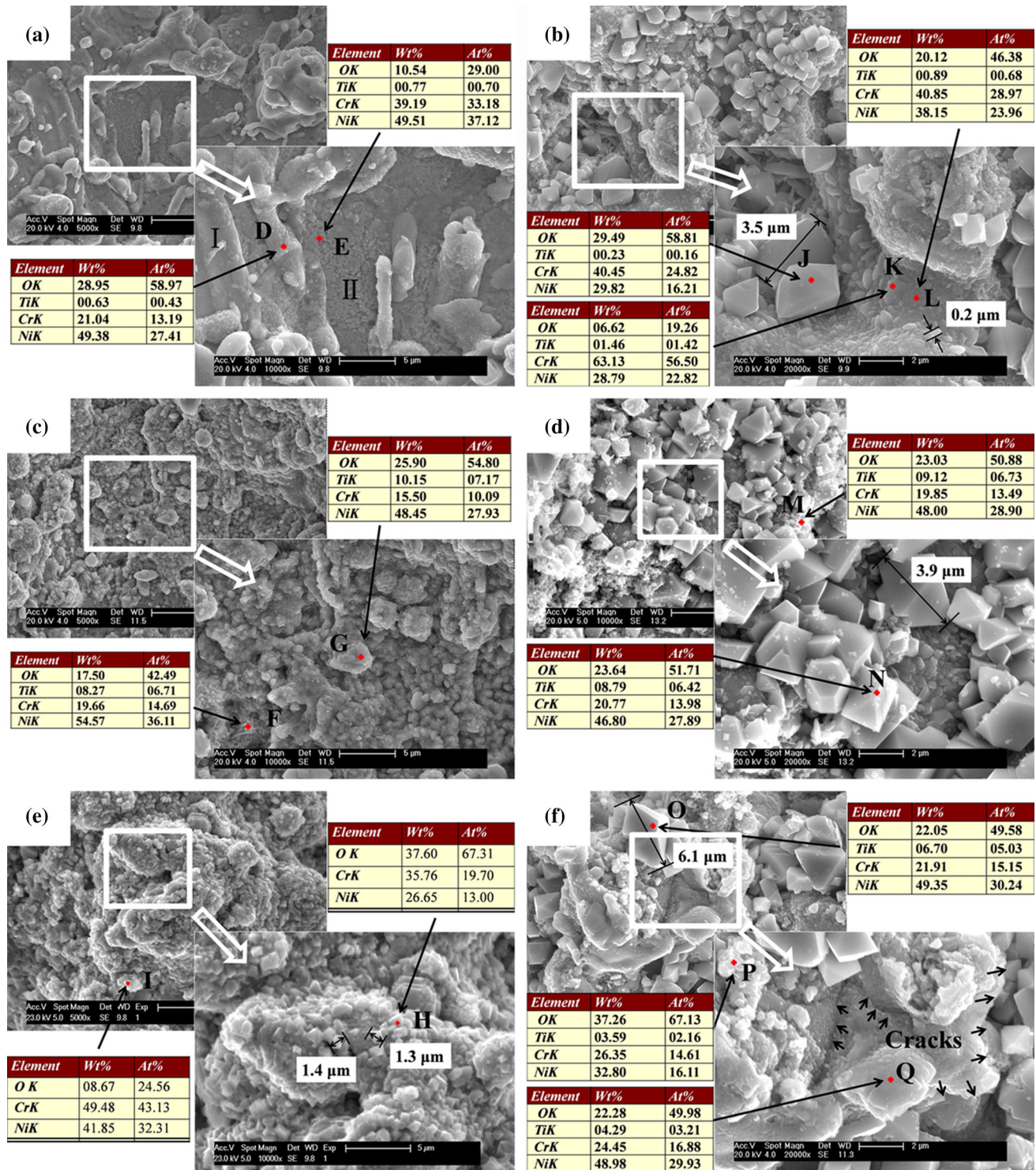


Fig. 5 SEM surface micrographs of the corroded specimens subjected to cyclic oxidation in air and hot corrosion under $\text{Na}_2\text{SO}_4 + \text{K}_2\text{SO}_4$ (7:3) mixed salt film at 550, 650, and 750 °C for 100 h. (a) Oxidation at 550 °C, (b) hot corrosion at 550 °C, (c) oxidation at 650 °C, (d) hot corrosion at 650 °C, (e) oxidation at 750 °C, (f) hot corrosion at 750 °C

usually form on the outer surface to cover $\text{NiO}/\text{Cr}_2\text{O}_3$ mixture and the Ni-Cr alloy substrate. The outer NiO phase is definitely stable due to the expose to air. However, the stability of NiO would decrease if it is located

inside due to the relatively lower oxygen activity. Therefore, the Ni atom in NiO will be replaced by Cr, and thus a continuous Cr_2O_3 would form. Simultaneously, NiO and Cr_2O_3 would react to form a spinel NiCr_2O_4 phase, which

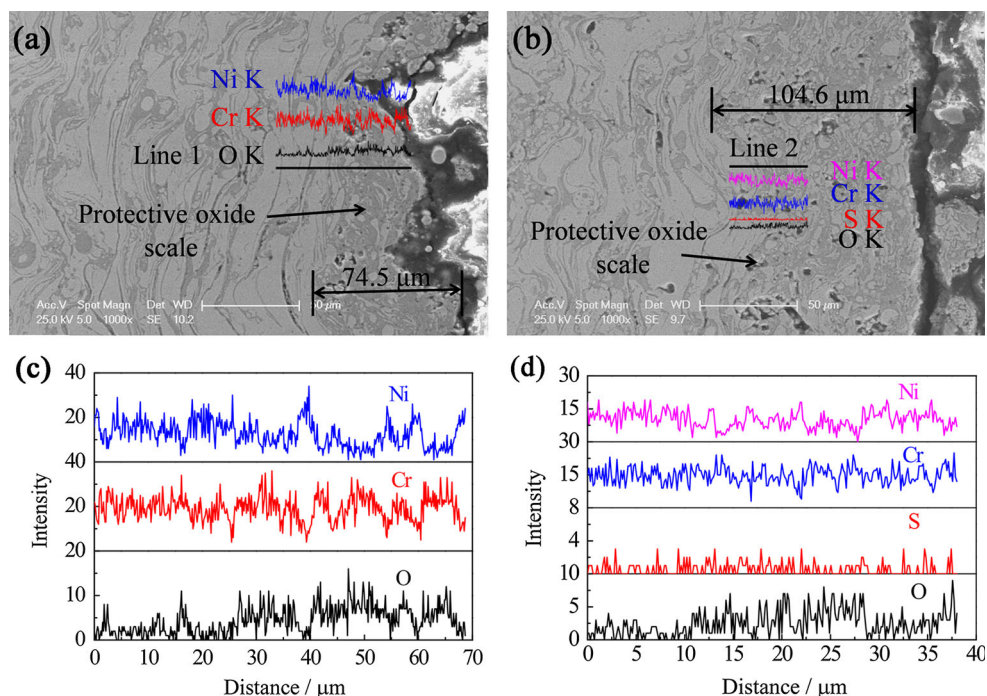


Fig. 6 Cross-sectional morphologies and EDS analysis of the oxide scale formed on the surface of corroded specimens after cyclic oxidation and hot corrosion at 650 °C for 100 h. (a) After oxidation, (b) after hot corrosion, (c) EDS analysis for line 1 in (a), (d) EDS analysis for line 2 in (b)

usually has smaller diffusion coefficients of the cations and anions than those in their parent oxides (Ref 24).

Figure 4 shows that the oxide scale formed on the 45 CT coatings after oxidation at 750 °C had a higher Cr_2O_3 and NiCr_2O_4 content than that formed at 550 or 650 °C. However, Fig. 3 shows that the coating has the lowest k_p value at 650 °C. Therefore, except the high content of Cr_2O_3 and NiCr_2O_4 in oxide scales, the dense and continuous microstructure of the oxide scale at 650 °C should also be taken as an important factor leading to the low increase rate in weight gain of the corroded 45CT coating (Fig. 5c). Similarly, the relatively higher k_p values at 550 and 750 °C compared to that at 650 °C could be attributed to the formation of a porous structure (Fig. 5a) and cracks or grooves in the oxide scales (Fig. 5e).

4.2 Hot Corrosion

Considering that the hot corrosion tests were conducted in air, the weight gain of the corroded specimens after hot corrosion could be ascribed to a combination of the sulfidation and successively oxidation effects, i.e., the sulfides of chromium and/or iron formed in the initial stage could be oxidized afterwards, and thus little S could be retained in the oxide scales as shown in Fig. 6d. Therefore, the EDS analysis results showed little S in the corrosion scale layer. Figure 7(c) and (d) shows the hot corrosion mechanism of the Ni-Cr-Ti coating under mixed sulfate film. The later oxidation behavior of the Ni-Cr-Ti coatings in the hot corrosion trials was similar as discussed in section 4.1.

Since the tested temperatures in this work were all lower than the melting points of Na_2SO_4 (m.p. 884 °C), K_2SO_4 (m.p. 1067 °C), and the mixture of $\text{Na}_2\text{SO}_4 + 30 \text{ wt.} \% \text{ K}_2\text{SO}_4$ (m.p. 815 °C), the corrosion should belong to the type of low temperature hot corrosion or type II hot corrosion (Ref 25, 26).

The low temperature hot corrosion mechanisms of Ni-Cr alloy induced by the deposition of sulphates were discussed attentively in the literature (Ref 12, 27–32). The eutectoid of $\text{Na}_2\text{SO}_4 + \text{Na}_2\text{O}$ (or $\text{K}_2\text{SO}_4 + \text{K}_2\text{O}$) with a low melting point of 550 °C would form in the sulphates-induced hot corrosion of Ni-Cr or Fe-Cr alloys (Ref 33–35). Therefore, the liquid phase of eutectoid of $\text{Na}_2\text{SO}_4 + \text{Na}_2\text{O}$ or $\text{K}_2\text{SO}_4 + \text{K}_2\text{O}$ could be expected to form in the temperature range of 550–750 °C used in the present study.

When the liquid phase of eutectoid formed on the surface of the corroded coatings, it probably could penetrate into the coatings in macro-scale liquid flow through pores or cracks. However, when the molten salt reached the protective oxides, these oxides would be dissolved into the molten salts based on the basic fluxing mechanism (Ref 29), as shown in Fig. 7(d). SO_4^{2-} can be reduced at the oxide-scale/molten-salts interface by the following Eq 1.



With the increasing activity of the O^{2-} , NiO can be dissolved in the molten salt by the Eq 2.



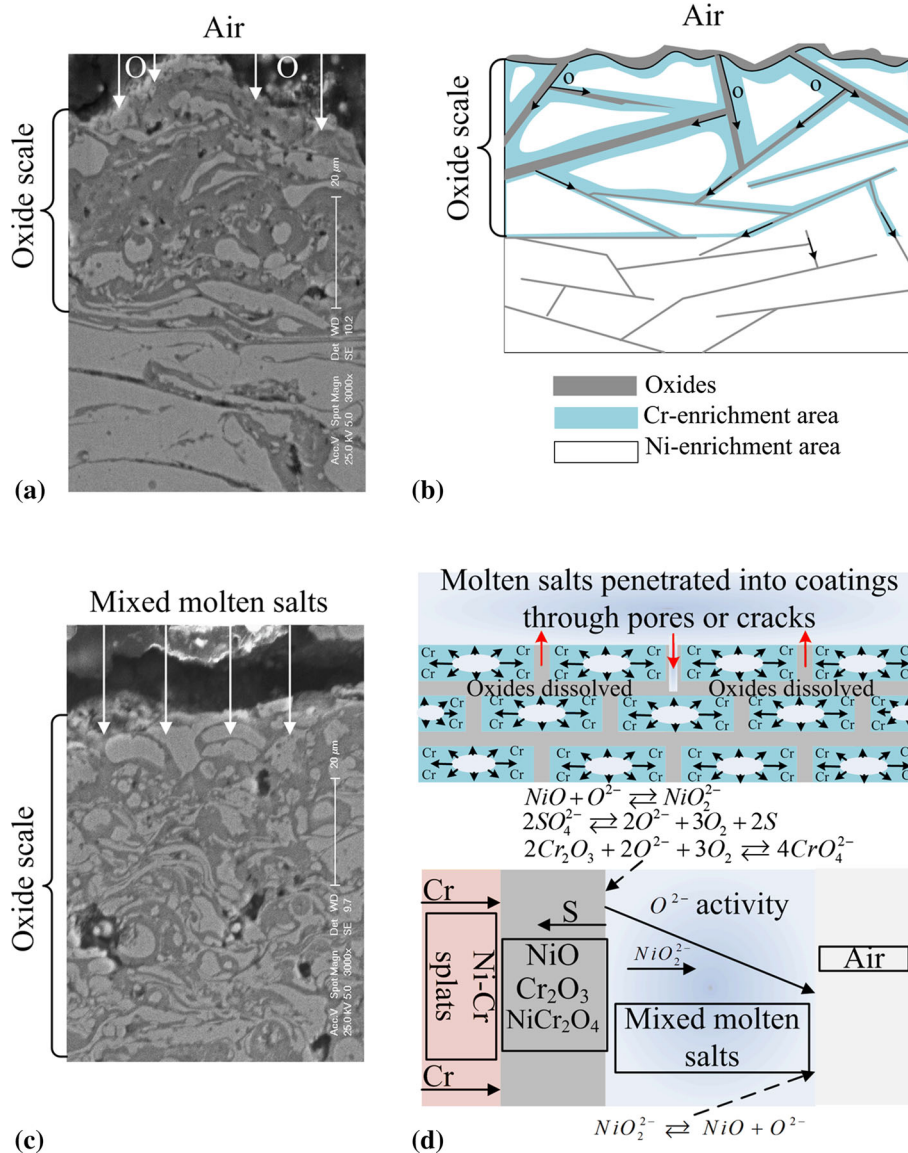


Fig. 7 A schematic diagram showing probable oxidation and hot corrosion model for arc-sprayed Ni-Cr coatings subjected to cyclic oxidation and hot corrosion at moderate temperatures. (a) Ni-43Cr-0.3Ti coating after oxidation at 650 °C; (b) oxidation model for (a); (c) Ni-43Cr-0.3Ti coating after sulfates-induced hot corrosion at 650 °C; (d) hot corrosion model for (c)

According to a “negative solubility gradient” proposed by Rapp and Goto (Ref 29), a continuous fluxing of the protective oxide scales will be proceeds as long as the negative solubility gradient of the oxides in the molten salts is valid. At the molten-salts/air interface, Eq 1 cannot be continued due to the high oxygen partial pressure (P_{O_2}). Due to the low activity of the O^{2-} , a reprecipitation of non-protective NiO is favored according to the opposite direction of Eq 2. However, the hot corrosion process of Ni-Cr coating can be effectively interrupted by the formation of chromia. This is mainly due to that the chromia can be preferentially reacts with O^{2-} at the oxide-scale/molten-salt interface by Eq 3.

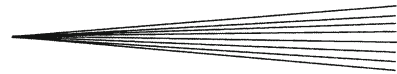


As the solubility of CrO_4^{2-} in the molten salts reached to a saturated state, hot corrosion process would be terminated.

That is the reason that chromia has been realized as the best oxide to resist hot corrosion in molten sulfates (Ref 29).

5. Conclusion

- (1) A high Cr content Ni-based coating, mainly composed of γ -Ni, Cr_2O_3 and NiO, was fabricated on the AISI 1020 steel substrate by the arc spray process. The coating showed a typical lamellar structure and a low a low porosity of 2.1%.
- (2) All the oxidation and hot corrosion kinetic curves of the coating at 550-750 °C agreed with a parabolic law. The parabolic rate constant for the hot corrosion was $7.2 \times 10^{-12} \text{ g}^2/(\text{cm}^4\cdot\text{s})$ at 650 °C, approximately 1.7 times higher than that for the oxidation at the same



temperature, indicating that the presence of sulfates significantly accelerated the high temperature deterioration process.

- (3) During the oxidation, the deterioration of the Ni-43Cr-0.3Ti coating was chemically controlled by the formation of oxides in the initial stage, such as NiO, Cr₂O₃, and NiCr₂O₄. As the protective oxide scale formed, it transformed to a diffusion controlled mode. However, as the liquid molten salts emerged during the hot corrosion, these protective oxides would be dissolved and the coating was corrupted acceleratedly.

Acknowledgments

The authors appreciate the financial supports from Fundamental Research Funds for the Central Universities (2013B34414, 2013B22814), National Natural Science Foundation of China (50979028), Natural Key Foundation of Jiangsu Province (BK2011025) and National 973 Plan Project (2015CB057803).

References

1. J. Nicholls, Advances in Coating Design for High-Performance Gas Turbines, *MRS Bull.*, 2003, **28**(9), p 659-670
2. C. Wagner, Theoretical Analysis of the Diffusion Processes Determining the Oxidation Rate of Alloys, *J. Electrochem. Soc.*, 1952, **99**(10), p 369-380
3. Z. Dong, X. Peng, Y. Guan, L. Li, and F. Wang, Optimization of Composition and Structure of Electrodeposited Ni-Cr Composites for Increasing the Oxidation Resistance, *Corros. Sci.*, 2012, **62**, p 147-152
4. D. Young, J. Zurek, L. Singheiser, and W. Quadackers, Temperature Dependence of Oxide Scale Formation on High-Cr Ferritic Steels in Ar-H₂-H₂O, *Corros. Sci.*, 2011, **53**(6), p 2131-2141
5. D.W. Yun, S. Seo, H. Jeong, I. Kim, and Y. Yoo, Modelling High Temperature Oxidation Behaviour of Ni-Cr-W-Mo Alloys with Bayesian Neural Network, *J. Alloy. Compd.*, 2014, **587**(25), p 105-112
6. N. Bala, H. Singh, S. Prakash, and J. Karthikeyan, Investigations on the Behavior of HVOF and Cold Sprayed Ni-20Cr Coating on T22 Boiler Steel in Actual Boiler Environment, *J. Therm. Spray Technol.*, 2012, **21**(1), p 144-158
7. S.S. Chatha, H.S. Sidhu, and B.S. Sidhu, High-Temperature Behavior of a NiCr-Coated T91 Boiler Steel in the Platen Superheater of Coal-Fired Boiler, *J. Therm. Spray Technol.*, 2013, **22**(5), p 838-847
8. N. Bala, H. Singh, and S. Prakash, Characterization and High-Temperature Oxidation Behavior of Cold-Sprayed Ni-20Cr and Ni-50Cr Coatings on Boiler Steels, *Metall. Mater. Trans. A*, 2011, **42**(11), p 3399-3416
9. F. Wang, X. Tian, Q. Li, L. Li, and X. Peng, Oxidation and Hot Corrosion Behavior of Sputtered Nanocrystalline Coating of Superalloy K52, *Thin Solid Films*, 2008, **516**(16), p 5740-5747
10. X. Ren and F. Wang, High-Temperature Oxidation and Hot-Corrosion Behavior of a Sputtered NiCrAlY Coating with and Without Aluminizing, *Surf. Coat. Technol.*, 2006, **201**(1), p 30-37
11. S. Kamal, R. Jayaganthan, and S. Prakash, Evaluation of Cyclic Hot Corrosion Behaviour of Detonation Gun Sprayed Cr₃C₂-25%NiCr Coatings on Nickel- and Iron-Based Superalloys, *Surf. Coat. Technol.*, 2009, **203**(8), p 1004-1013
12. N. Bala, H. Singh, and S. Prakash, Accelerated Hot Corrosion Studies of Cold Spray Ni-50Cr Coating on Boiler Steels, *Mater. Des.*, 2010, **31**(1), p 244-253

13. T. Sidhu, S. Prakash, and R. Agrawal, Evaluation of Hot Corrosion Resistance of HVOF Coatings on a Ni-Based Superalloy in Molten Salt Environment, *Mater. Sci. Eng. A*, 2006, **430**(1), p 64-78
14. H. Singh, D. Puri, and S. Prakash, Some Studies on Hot Corrosion Performance of Plasma Sprayed Coatings on a Fe-Based Superalloy, *Surf. Coat. Technol.*, 2005, **192**(1), p 27-38
15. W. Zanchuk, The Use of Tafaloy 45CT, an Ni-Cr-Ti Alloy, as an Arc Sprayed Corrosion Barrier in High Temperature Sulfurous Environments, *Surf. Coat. Technol.*, 1989, **39-40**(Part 1), p 65-69
16. S. Matthews and M. Schweizer, Optimization of Arc-Sprayed Ni-Cr-Ti Coatings for High Temperature Corrosion Applications, *J. Therm. Spray Technol.*, 2013, **22**(4), p 538-550
17. V. Shukla, R. Jayaganthan, and V. Tewari, Environmental Degradation Behavior of High-Velocity Arc Sprayed FeCrBMnSi Alloy Coatings in a Coal Fired Boiler, *Acta Metall. Sin.*, 2013, **26**(5), p 602-612
18. S. Matthews and M. Schweizer, High-Temperature Oxidation and Melt Deposit Corrosion of Ni-Cr-Ti Arc-Sprayed Coatings, *J. Therm. Spray Technol.*, 2013, **22**(6), p 932-946
19. G. Calvarin, R. Molins, and A. Huntz, Oxidation Mechanism of Ni-20Cr Foils and Its Relation to the Oxide-Scale Microstructure, *Oxid. Met.*, 2000, **53**(1-2), p 25-48
20. G. Calvarin-Amiri, A. Huntz, and R. Molins, Effect of an Applied Stress on the Growth Kinetics of Oxide Scales Formed on Ni-20Cr Alloys, *Mater. High Temp.*, 2001, **18**(2), p 91-99
21. R. Viswanathan, J. Sarver, and J. Tanzosh, Boiler Materials for Ultra-Supercritical Coal Power Plants-Steamside Oxidation, *J. Mater. Eng. Perform.*, 2006, **15**(3), p 255-274
22. S. Mrowec, On the Mechanism of High Temperature Oxidation of Metals and Alloys, *Corros. Sci.*, 1967, **7**(9), p 563-578
23. S. Saunders, M. Monteiro, and F. Rizzo, The Oxidation Behaviour of Metals and Alloys at High Temperatures in Atmospheres Containing Water Vapour: A Review, *Prog. Mater. Sci.*, 2008, **53**(5), p 775-837
24. U. Chatterjee, S.K. Bose, and S.K. Roy, *Environmental Degradation of Metals: Corrosion Technology Series/14*, CRC Press, Marcel Dekker Inc, New York, 2001
25. S.J. Geng, F.H. Wang, S.L. Zhu, and W. Wu, Hot-Corrosion Resistance of a Sputtered K38G Nanocrystalline Coating in Molten Sulfate at 900 °C, *Oxid. Met.*, 2002, **57**(5-6), p 549-557
26. L. Shi, Y. Zhang, and S. Shi, The Effect of K₂SO₄ Additive in Na₂SO₄ Deposits on Low Temperature Hot Corrosion of Iron-Aluminum Alloys, *Oxid. Met.*, 1992, **38**(5-6), p 385-405
27. T. Sidhu, S. Prakash, and R. Agrawal, Hot Corrosion and Performance of Nickel-Based Coatings, *Curr. Sci. Bangalore*, 2006, **90**(1), p 41-47
28. T. Sidhu, S. Prakash, and R. Agrawal, Hot Corrosion Performance of a NiCr Coated Ni-Based Alloy, *Scripta Mater.*, 2006, **55**(2), p 179-182
29. R.A. Rapp, Hot Corrosion of Materials: A Fluxing Mechanism?, *Corros. Sci.*, 2002, **44**(2), p 209-221
30. G. Mahobia, N. Paulose, and V. Singh, Hot Corrosion Behavior of Superalloy IN718 at 550 and 650 °C, *J. Mater. Eng. Perform.*, 2013, **22**(8), p 2418-2435
31. J. Goebel, F. Pettit, and G. Goward, Mechanisms for the Hot Corrosion of Nickel-Base Alloys, *Metall. Mater. Trans. B*, 1973, **4**(1), p 261-278
32. T. Sidhu, S. Prakash, and R. Agrawal, Hot Corrosion Studies of HVOF Sprayed Cr₃C₂-NiCr and Ni-20Cr Coatings on Nickel-Based Superalloy at 900 °C, *Surf. Coat. Technol.*, 2006, **201**(3), p 792-800
33. K. Tao, X.-L. Zhou, H. Cui, and J.-S. Zhang, Oxidation and Hot Corrosion Behaviors of HVOF-Sprayed Conventional and Nanostructured NiCrC Coatings, *Trans. Nonferr. Met. Soc. China*, 2009, **19**(5), p 1151-1160
34. K. Tao, X. Zhou, H. Cui, and J. Zhang, Preparation and Properties of a Nanostructured NiCrC Alloy Coating for Boiler Tubes Protection, *Mater. Trans.*, 2008, **49**(9), p 2159-2162
35. L. Shi, Accelerated Oxidation of Iron Induced by Na₂SO₄ Deposits in Oxygen at 750 °C—A New Type Low-Temperature Hot Corrosion, *Oxid. Met.*, 1993, **40**(1-2), p 197-211